ChemCatChem

Research Article
doi.org/10.1002/cctc.202500595

Chemistry Europe
European Chemical Societies Publishing

www.chemcatchem.org

# Noble Metal-Supported $CeO_2$ Catalysts for Hydrogen Production via Ethanol Steam Reforming

Felipe Anchieta e Silva,[a] Eduardo do Espírito Santo Marques,[a] Fabio Coral Fonseca,[b] Aleksander Gurlo,[c] and Thenner Silva Rodrigues*[a, c]

This study investigates the synthesis, characterization, and catalytic performance of noble metal-supported cerium oxide ($M/CeO_2$, where M = Au, Pd, Pt, Rh, Ru) catalysts for ethanol steam reforming, a promising method for sustainable hydrogen production. A urea-assisted deposition approach was employed to deposit noble metal nanoparticles uniformly on $CeO_2$ without stabilizers, preserving the support's crystallinity and enhancing reducibility through strong metal-support interactions. Catalytic tests at 550 °C over 24 h revealed significant differences in activity and the products distribution based on the metal used. $Rh/CeO_2$ demonstrated the highest performance, achieving complete ethanol conversion and 37.75% hydrogen production, attributed to its efficient C—C and C—H bond cleavage. $Pt/CeO_2$ and $Ru/CeO_2$ also displayed high activity and stability, whereas $Pd/CeO_2$ and $Au/CeO_2$ primarily produced acetaldehyde due to preferential C—H bond scission. Post-reaction analysis confirmed minimal carbon deposition across all catalysts, with $Rh/CeO_2$ exhibiting the highest resistance to coke formation. These findings emphasize the importance of noble metal choice and metal-support interactions in optimizing catalyst performance. Rh, Pt, and Ru emerged as the most promising candidates for efficient hydrogen production. This study develops advanced catalysts optimized for renewable energy use for hydrogen production via ethanol steam reforming.

## 1. Introduction

Hydrogen is utilized globally across various industries for a wide range of applications. It is predominantly produced from fossil fuels through processes such as methane steam reforming, gasification, partial oxidation of heavy oil, and steam reforming reactions.[1–4] Hydrogen is considered a next-generation energy source due to its high energy potential and its capacity to reduce environmental impact.[2,5] In this context, reducing pollutant emissions and mitigating global warming made hydrogen production from ethanol an attractive and efficient alternative. Biomass-derived ethanol is a readily available and efficient fuel with well-developed infrastructure for production and distribution, especially in countries like the USA and Brazil.[4] Ethanol is already a well-established biofuel for combustion engines, and recent interest has grown in using ethanol in fuel cells and as a renewable source for hydrogen production.[6–8]

Ethanol steam reforming produces hydrogen ($H_2$) and carbon dioxide ($CO_2$) as primary products.[9] However, under real experimental conditions, not only the stoichiometric reaction occurs to produce $H_2$ and $CO_2$; various side reactions, such as ethanol dehydrogenation, dehydration, decomposition, and coke deposition, can also take place, leading to a mixture of compounds.[9–11] Numerous studies have shown that $H_2$ selectivity and the formation of other compounds can be controlled by systematically adjusting process parameters, such as temperature, stoichiometry of the reactants, gas hourly space velocity (GHSV), and the choice of catalyst.[10–13] To enhance the catalytic reaction, nanocatalysts have been used as supported catalysts, structured with an active phase and solid support. The active phase directs the reaction, with metals like Ni,[12] Co,[14] Au,[15] Ir,[16] Pd,[17] Pt,[18,19] Rh,[20] and Ru[21] commonly employed. Non-noble metals offer a low-cost option with great potential; however, they tend to have lower activity, selectivity, and stability, often deactivating after a short reaction time.

Non-noble metal catalysts exhibit deactivation within few hours (<10 h) of operation due to rapid carbon deposition and thermal sintering, depending on the active phase and support.[22,23] The economically attractive catalysts often require frequent regeneration cycles, with complete deactivation occurring in less than 24 h under aggressive reforming conditions. In contrast, noble metal catalysts demonstrate superior stability, maintaining activity for more than 24 h due to their inherent resistance to coking and thermal degradation.[20,24,25] Although the high initial cost of noble metals presents a significant barrier, their extended operational lifetime, higher hydrogen selectivity (>70% versus <60% for non-noble metals), and reduced downtime justify their use in continuous industrial applications.[20,24,25] The price premium is partially offset by lower replacement frequency and maintenance costs, making noble metals particu-

[a] F. A. e Silva, E. do E. S. Marques, T. S. Rodrigues
Nanotechnology Engineering Program, Alberto Luiz Coimbra Institute for Graduate Studies and Research in Engineering, COPPE, Federal University of Rio de Janeiro, Av. Horácio Macedo, 2030, Rio de Janeiro RJ 21941–972, Brazil
E-mail: thenner@pent.coppe.ufrj.br

[b] F. C. Fonseca
Instituto de Pesquisas Energéticas e Nucleares, IPEN/CNEN-SP, Av. Prof. Lineu Prestes, 2242, São Paulo, São Paulo 05508-000, Brazil

[c] A. Gurlo, T. S. Rodrigues
Faculty III Process Sciences, Institute of Materials Science and Technology, Chair of Advanced Ceramic Materials, Technische Universität Berlin, Straße des 17. Juni 135, Berlin 10623, Germany

larly advantageous for large-scale hydrogen production facilities where process reliability is paramount.

In contrast, noble metals exhibit high activity, selectivity, stability, and resistance to deactivation and coke deposition. The catalytic reaction is among the one of the most sustainable methods for $H_2$ production. To enhance the sustainability, availability, and productivity of $H_2$. In previous work, we demonstrated the influence of different supports ($CeO_2$, $TiO_2$, $SiO_2$, ZnO, and $Al_2O_3$) on ethanol steam reforming, which explored the influence of oxide supports in this reaction, demonstrating that $CeO_2$ is the best support in terms of $H_2$ production, ethanol conversion, and stability.[20] The reaction was conducted with an $H_2O/CH_3CH_2OH$ molar ratio of 3 (theoretical stoichiometric ratio, Equation 1), at 550 °C, which offers optimal ethanol conversion and $H_2$ formation, for a continuous 24 h period.

$$CH_3CH_2OH_{(ads)} + 3H_2O_{(ads)} \rightarrow 6H_{2(g)} + 2CO_{2(g)} \quad (1)$$

In this study, our focus was to improve the catalyst performance for ethanol steam reforming and to understand the role of noble metals as the active phase due to selectivity and stability were strongly affected by the nature of the catalytic support, which promoted different reactions, such as ethanol steam reforming, dehydration, decomposition, and dehydrogenation. $CeO_2$ showed particularly good selectivity, stability, and resistance to deactivation and coke deposition. In this study, we aim to understand the effect of noble metals on the performance of $M/CeO_2$ catalysts (where M = Au, Pd, Pt, Rh, and Ru) for ethanol steam reforming. We first employed a urea-assisted deposition protocol, which facilitated the reduction of $M^{n+}$ to $M^0$ and its incorporation onto the commercial $CeO_2$ support without using any stabilizers or capping agents. After synthesis and characterization, the catalytic performance of the $M/CeO_2$ catalysts was investigated in ethanol steam reforming, chosen as a model reaction due to its importance in hydrogen production from renewable raw materials. Our primary focus was to investigate how different active phases influence the performance of nanocatalysts in terms of activity, selectivity, and stability.

## 2. Materials and Methods

### 2.1. Materials

Analytical grade cerium (IV) oxide ($CeO_2$, 99.9%, Evonik), gold(III) chloride ($HAuCl_4$, 99.5%,Sigma-Aldrich), palladium(II) chloride ($PdCl_2$, 99.5%, Sigma-Aldrich), platinum(IV) chloride ($PtCl_4$, 99.5%, Sigma-Aldrich), rhodium (III) chloride ($RhCl_3$, 99.99%, Sigma-Aldrich), ruthenium(III) chloride ($RuCl_3$, 99.5%, Sigma-Aldrich), urea ($CH_4N_2O$, 99.75%, Vetec), ethanol ($C_2H_6O$, 99.5%, Sigma-Aldrich), and silicon carbide (SiC, 99.99%, Sigma-Aldrich), hydrochloric acid (HCl, 37%, Vetec), and nitric acid ($HNO_3$, 70%, Vetec), were used as received. All glassware was cleaned with aqua regia (HCl: $HNO_3$ = 3:1) before the synthesis to prevent contamination.

### 2.2. Synthesis of $M/CeO_2$ (M = Au, Pd, Pt, Rh, and Ru) Catalysts

The metal nanoparticles deposition on $CeO_2$ was carried out using a deposition-precipitation method assisted by urea[26,27] aiming target a metal loading of 0.5%. In a round-bottomed flask, 2.0 g $CeO_2$ was dispersed in 100.0 mL Milli-Q water and ultrasonicated for 15 min. Then, the suspension was stirred magnetically for 15 min at 90 °C in an oil bath. Subsequently, 0.6 g urea was added to the suspension and 400 µL of the aqueous precursor solution at 25 mM was added dropwise (1 drop per second) and maintained under stirring at 90 °C for 4 h. After that period, the glassware was removed from the oil bath to naturally cool down at room temperature. The solid was centrifugated at 10,000 rpm for 10 min for three times with Milli-Q water to remove contaminants such as $Cl^-$ ions, residual urea, and unreacted metal ions, and twice with ethanol to improve the drying process at 110 °C for 2 h. The solid was calcined in air at 500 °C for 2 h with a heating rate of 10 °C $min^{-1}$. The calcination temperature was selected based on TGA analysis and Raman spectroscopy as previous reported.[20]

### 2.3. Characterization Methods

Scanning electron microscopy (SEM) images were obtained using a Tescan VEGA 3 LMU operated at 20 kV. The samples were not pretreated before SEM analysis; they were dispersed in a 50% ethanol/water mixture and ultrasonicated for 15 min. Then, the suspension was drop-cast onto a silicon wafer and dried under ambient conditions. Before SEM analysis, the silicon wafer was washed with deionized water to prevent contamination.

Transmission electron microscopy (TEM) images were obtained with a JEOL JEM-1011 microscope operated at 100 kV. The samples were then dispersed in a 50% ethanol/water mixture, ultrasonicated for 15 min, and dropped cast onto a carbon-coated copper grid, followed by drying under ambient conditions.

Energy dispersive X-ray spectroscopy (EDS) was used for elemental mapping with a Tescan VEGA 3 LMU scanning electron microscope operated at 20 kV. The noble metal weight percentages were measured using inductively coupled plasma optical emission spectrometry (ICP-OES) on a Spectro Arcos instrument.

Specific surface areas were determined by the Brunauer-Emmett-Teller (BET) method using a Quantachrome ChemBET-Pulsar instrument with a thermal conductivity detector. Typically, 0.05 g of catalyst was pretreated with He flow at 300 °C for 3 h and then cooled to room temperature.

Temperature-programmed reduction with hydrogen ($H_2$-TPR) and CO chemisorption studies were conducted on the Quantachrome ChemBET-Pulsar instrument. For TPR, 0.05 g of catalyst was dried with He flow at 200 °C for 20 min, cooled to room temperature, and then heated between 50 and 1100 °C in a 10% $H_2/N_2$ flow, with a temperature increase rate of 10 °C·$min^{-1}$. The reducibility of the catalysts was determined from the ratio between the hydrogen consumption area below 500 °C and the total hydrogen consumption area (Equation 2). CO chemisorp-

tion and Temperature-Programmed Desorption (CO-TPD) were performed on both fresh and spent catalysts. The exposed Rh area was measured by CO pulse chemisorption at 50 °C with pulses of 5% CO in He. Prior to chemisorption, 0.05 g of catalyst was pretreated at 450 °C under a 10% $H_2/N_2$ flow, with a 10 °C·min$^{-1}$ temperature increase rate, held at 450 °C for 1 h, and then cooled to 50 °C. CO-TPD was performed by heating in a He stream at 75 cm$^3$·min$^{-1}$ between 50 and 1100 °C with a heating rate of 10 °C·min$^{-1}$. The metal dispersion was calculated from accessible active phase measured via CO-TPD and total metal content obtained from ICP-OES analysis (Equation 3).

$$\text{Reducibility } (\%) = \frac{\text{Area}_{\text{until } 500^\circ\text{C}}}{\text{Total Area}} \times 100 \quad (2)$$

$$\text{Dispersion } (\%) = \frac{\text{Accessible active phase } (\text{mol}_{\text{metal}})}{\text{Total metal content } (\text{mol}_{\text{metal}})} \quad (3)$$

The metal weight percentages were measured by inductively coupled plasma optical emission spectrometry (ICP-OES) using a Spectro Arcos equipment.

X-ray diffraction (XRD) data were obtained using Rigaku-Miniflex II equipment with Cu K$\alpha$ radiation. Diffraction patterns were measured in the range of 20°−90° 2$\theta$ with a scan speed of 1°·min$^{-1}$.

Thermogravimetric (TGA) measurements were performed on Setaram-LabSys equipment over a temperature range of 25–1000 °C with a heating rate of 5 °C·min$^{-1}$ under synthetic air flow. Before analysis, samples were pretreated under vacuum at 25 °C for 1 h.

Raman spectra were collected using a Renishaw InVia Reflex spectrometer coupled with a Leica DM 2500 M microscope and a CCD detector. Laser excitation at 632.8 nm (He/Ne source) was used with a 50× objective lens (NA = 0.9).

### 2.4. Catalytic Experiments: Ethanol Steam Reforming

Catalytic experiments were conducted under atmospheric pressure in a fixed-bed quartz tubular reactor with a 5 mm inner diameter. The reactor was packed with quartz wool and 100 mg of catalyst powder diluted with silicon carbide (SiC). The reactor was placed in a vertical oven equipped with a thermocouple to control the temperature at 550 °C. Before reaction, the catalysts were reduced under pure $H_2$ atmosphere at 400 °C for 1 h, at a f low rate of 50 mL·min$^{-1}$. The reduction temperature was determined through the $H_2$–TPR (Figure 5). Water and ethanol ($CH_3CH_2OH$) steam were generated using two bubblers: one containing water and the other ethanol, to obtain a $H_2O/CH_3CH_2OH$ molar ratio of 3 and fed into the reactor.

The feed composition (assessed via ethanol vapor pressure, $P_{\text{feed}}$) was determined by Antoine's equation (Equation 4) with parameters: water (A = 4.65, B = 1435.26, C = −64.85, and $T$ = 65 °C) and ethanol ($A$ = 5.37, $B$ = 1670.41, $C$ = −40.19, and $T$ = 15 °C), and Raoult's law ($P_{\text{atm}}$ = 1.0,1325 bar) (Equation 5). The He inlet flow rates of the individual gas streams were controlled with mass flow meters (MKS Instruments) ranging from 10 mL·min$^{-1}$ to ethanol and from 10 mL·min$^{-1}$ to water, obtaining a total flow rate from 20 mL·min$^{-1}$. The reactants and reaction products were analyzed using a gas chromatography system (GC-2014 Shimadzu) equipped with two columns. The first column, an Rtx-Plot-Q (30 m, 0.32 mm i.d.), separated the heavier products, which were then analyzed by an FID. The lighter compounds, primarily $H_2$, CO, and $CO_2$, cannot be detected by the FID. To address this, the FID outlet stream was passed through a cold trap and then directed into another column (Carboxen 1010, 30 m, 0.53 mm i.d.) before being analyzed by a TCD. The tubes were maintained at 120 °C, with thermocouples monitoring multiple sections to prevent condensation, fouling, and cold spots. Data processing was performed using software integrated with the chromatograph (GCSolution, v. 2.32), which enabled real-time monitoring of catalytic performance.

$$\log P_{\text{feed}} = A - \frac{B}{T + C} \quad (4)$$

$$P_{\text{feed}} = X_{\text{feed}} \times P_{\text{atm}} \quad (5)$$

The analytic calibration curve was determined for ethanol ($CH_3CH_2OH$), hydrogen ($H_2$), carbon dioxide ($CO_2$), carbon monoxide (CO), methane ($CH_4$), acetone ($CH_3(CO)CH_3$), acetaldehyde ($CH_3CHO$), ethene ($C_2H_4$), ethane ($C_2H_6$), propene ($C_3H_6$), and propane ($C_3H_8$). The calibration curve was established using 5 points. The liquids were calibrated using a bubbler and the mole fraction was adjusted by varying the bubbler temperature determined via Antoine equation (Equation 4), Raoult's law (Equation 5), and ideal gas law. Additionally, the molar fraction of the gases was adjusted by diluting them with the He carrier gas. The catalytic performance was assessed based on ethanol conversion profiles ($X_{EtOH}$), as described in Equation (6). Here, $X_{EtOH}$ represents the observed ethanol conversion, calculated using the inlet ($\text{mol}_{EtOH,in}$) and outlet ($\text{mol}_{EtOH,out}$) ethanol flow rates. Products distribution ($S_i$) was evaluated as a function of the reaction time as in Equation (7), where $S_i$ refers to the product distribution of species i and $C_i$ is the concentration of species i. The denominator represents the total concentration of all detected species at the reactor outlet, like hydrogen ($H_2$), carbon dioxide ($CO_2$), carbon monoxide (CO), methane ($CH_4$), acetone ($CH_3(CO)CH_3$), acetaldehyde ($CH_3CHO$), and ethene ($C_2H_4$).

$$X_{\text{EtOH}}\,[\%] = \frac{\left(\text{mol}_{\text{EtOH, in}} - \text{mol}_{\text{EtOH, out}}\right)}{\text{mol}_{\text{EtOH, in}}} \times 100 \quad (6)$$

$$S_i\,[\%] = \frac{C_i}{\sum_{m=1}^{n} C_i} \quad (7)$$

## 3. Results and Discussion

Our investigation began by selecting commercial $CeO_2$ as the support for the desired catalysts to avoid additional support effects and focus solely on the metal's effect on the catalytic reaction. SEM images of $CeO_2$, depicted a large particle size distribution with average size corresponding to 16.7 µm with

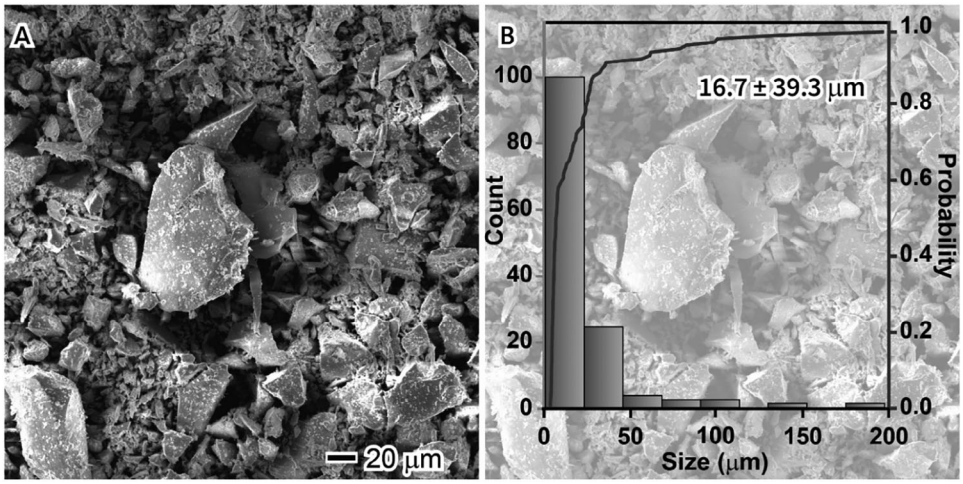


**Figure 1.** (A) SEM images and (B) particle size distribution for the $CeO_2$ pure support.

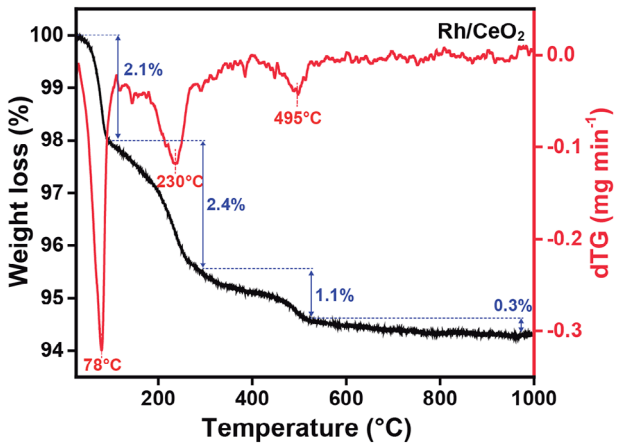


**Figure 2.** TGA-dTG plot for $Rh/CeO_2$ catalyst.

non-controlled morphology (Figure 1). Then, the synthesis of catalysts described as $M/CeO_2$ (where M = Au, Pd, Pt, Rh, and Ru) were synthesized using a chemical reduction method, in which metal nanoparticles deposition-precipitation was achieved in a single step, with urea serving as the reducing agent. The calcination temperature was determined via TGA analysis, as depicted in Figure 2.

The thermal decomposition of urea, which takes place in two stages. The first stage, occurring at 238 °C, involves the breakdown of urea into ammonia and isocyanic acid, as described in (Equation 8).[28] The second stage, at 388 °C, involves isocyanic acid reacting with water to produce ammonia and $CO_2$ (Equation 9), with complete decomposition achieved at 500 °C, which was determined the calcination temperature of $M/CeO_2$ catalysts.[20]

$$CO(NH_2)_2 \rightarrow NH_{3(g)} + HNCO_{(g)} \quad (8)$$

$$HNCO_{(g)} + H_2O_{(g)} \rightarrow NH_{3(g)} + CO_{2(g)} \quad (9)$$

Figure 3 displays the scanning electron microscopy (SEM), energy-dispersive X-ray spectroscopy (SEM-EDX), transmission electron microscopy (TEM) images, and particle size distribution for the $M/CeO_2$ catalysts, where M represents Au, Pd, Pt, Rh, and Ru. The images are organized as follows: $Au/CeO_2$ (Figures 3A–E), $Pd/CeO_2$ (Figures 3F–J), $Pt/CeO_2$ (Figures 3K–O), $Rh/CeO_2$ (Figures 3P–T), and $Ru/CeO_2$ (Figures 3U–Y), respectively. The SEM images in the first column revealed that for all $M/CeO_2$ samples, the $CeO_2$ support kept unchanged initial characteristics such as poor control over the shape and size of the support particles. Herein, no significant morphological changes were observed in the $CeO_2$ support after metal deposition compared to pure $CeO_2$ (Figure 1). In the second column, low-magnification SEM-EDX images revealed a uniform distribution of metal nanostructures (depicted in green) across the support surfaces (shown in yellow). This uniform dispersion increases the accessible metal surface area, leading to improved catalytic activity. This achievement reflects a well-regulated synthesis process. The third column presents TEM images, and the fourth column depicts the particle size distribution of the $M/CeO_2$ catalysts. The $CeO_2$ support consists of micro-sized particles, as shown in Figure 1. However, TEM images reveal that these particles are composed of $CeO_2$ crystallites with an average size of 5.8 nm, which is consistent with the crystallite size reported in Table 1. Due to the structure of $CeO_2$, the metal nanoparticles can be identified by differences in mass-thickness and electronic density, as indicated by green arrows. As also shown in Table 1, the metal nanoparticles have average sizes of 5.9 nm for $Au/CeO_2$ (Figure 3D), 5,7 nm for $Pd/CeO_2$ (Figure 3I), 3.7 nm for $Pt/CeO_2$ (Figure 3N), 2.6 nm for $Rh/CeO_2$ (Figure 3S), and 4.7 nm for $Ru/CeO_2$ (Figure 3X).

Figure 4 presents the X-ray diffraction (XRD) for the $M/CeO_2$ catalysts (M = Au, Pd, Pt, Rh, Ru). The XRD profiles displayed well-defined and intense peaks corresponding to the face-centered cubic (*fcc*) fluorite structure of $CeO_2$, with no detectable contaminants or secondary phases. The diffraction peaks align with $2\theta$ values of 28° (111), 33° (200), 47° (220), 56° (311), 58° (222), 69° (400), 76° (331), 79° (420), and 88° (422), confirming the crystalline phase of the materials.[29,30] Notably, the XRD patterns of the $M/CeO_2$ catalysts showed no significant differences compared to pure $CeO_2$, indicating that the deposition of noble metals

Research Article
doi.org/10.1002/cctc.202500595

Chemistry Europe
European Chemical Societies Publishing

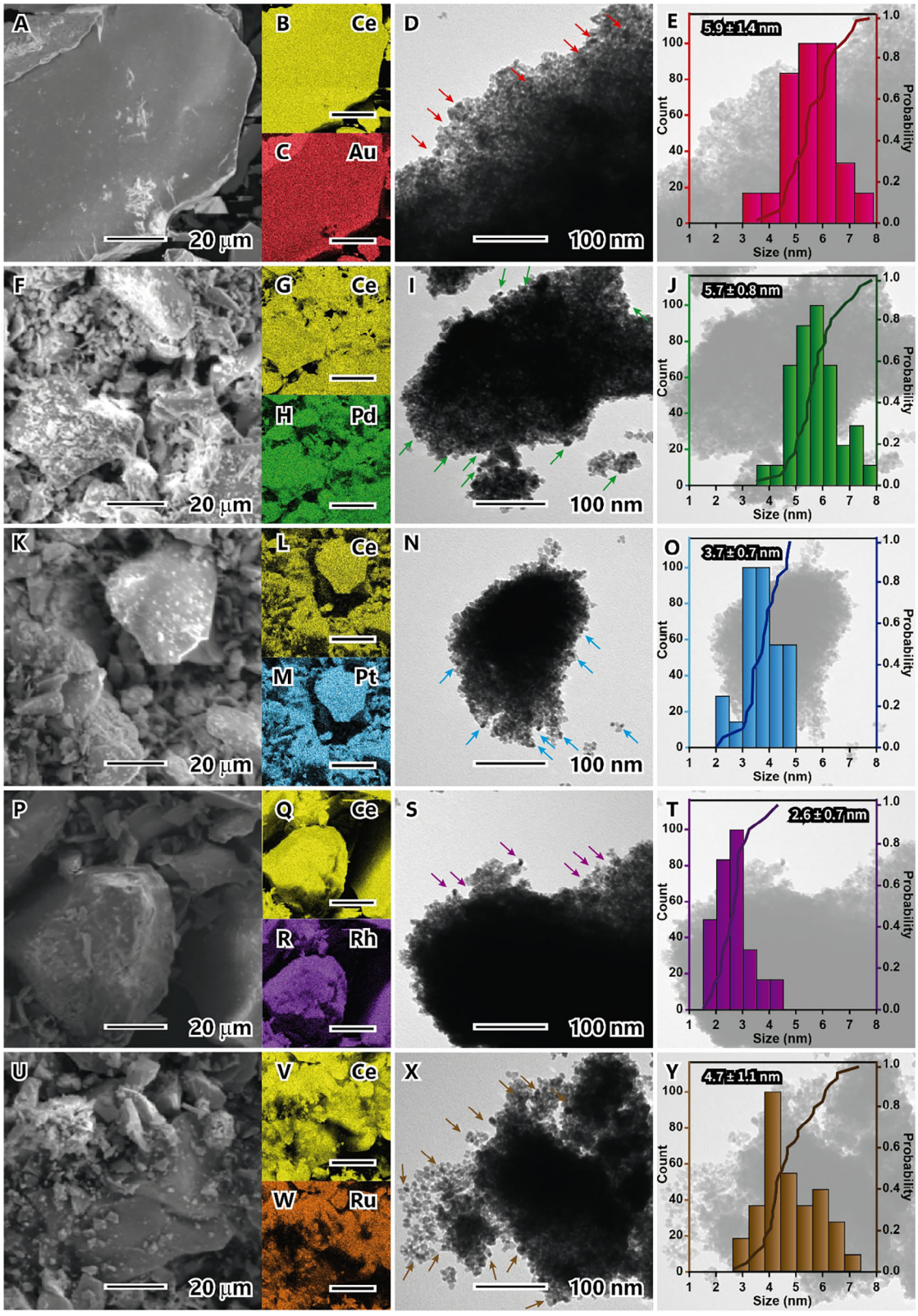


**Figure 3.** SEM (first column), SEM-EDX elemental map (second column), TEM (third column) images, and particle size distribution (fourth column) for the (A-E) Au/$CeO_2$, (F-J) Pd/$CeO_2$, (K-O) Pt/$CeO_2$, (P-T) Rh/$CeO_2$, (U-Y) and Ru/$CeO_2$. The scale bar at SEM-EDX map corresponds 20 μm.

**Table 1.** Physical and chemical properties of $CeO_2$ and $M/CeO_2$ catalysts.

| Sample | Particle Size (nm) | Crystallite Size (nm) | Specific Surface Area ($m^2 \cdot g^{-1}$) | Metal content (wt%) | Specific Metal Surface Area ($m^2 \cdot g^{-1}$) | Dispersion (%) | Reducibility (%) |
|---|---|---|---|---|---|---|---|
| $CeO_2$ | 16696 | 6.0 | 85.9 | – | – | – | 9.9 |
| $Au/CeO_2$ | 5.9 | 5.7 | 81.3 | 0.3 | 0.3 | 24.1 | 19.6 |
| $Pd/CeO_2$ | 4.6 | 5.6 | 91.4 | 0.2 | 0.2 | 15.4 | 45.1 |
| $Pt/CeO_2$ | 3.7 | 5.7 | 122.6 | 0.2 | 0.1 | 21.5 | 41.3 |
| $Rh/CeO_2$ | 2.6 | 5.4 | 77.4 | 0.3 | 0.3 | 29.7 | 33.7 |
| $Ru/CeO_2$ | 4.7 | 5.5 | 95.9 | 0.1 | 0.1 | 17.8 | 76.5 |

and the subsequent thermal treatment did not affect the structural integrity of the $CeO_2$ support. This was further supported by crystallite size calculations using Scherrer's equation, which ranged from 5.4 to 6.0 nm (Table 1). These findings are consistent with TEM images (Figure 3), which confirm the nanoparticulate nature of the $CeO_2$ support. Peaks corresponding to metal-based species were not detected, likely due to the small size and low metal loading of the noble metal nanoparticles. An exception was observed for $Au/CeO_2$, where a peak at 38° was identified, corresponding to the (111) plane of the Au *fcc* phase.[31,32]

Table 1 depicts the metal loadings as determined by ICP-OES, particle size as determined by TEM images, crystallite size as determined by XRD profiles, specific surface areas as determined by $N_2$ physisorption, metal surface areas and dispersions as measured by CO chemisorption, and catalyst reducibility as measured by $H_2$-TPR. Initially, the metal content was targeted to be 0.5% due to the high cost to noble metals and some papers reported noble-metal catalysts using 0.5% metal content depicted high ethanol conversion and hydrogen production.[9,13,33,34] However, the metal contents in $M/CeO_2$ determined by ICP-OES were 0.3%, 0.2%, 0.2%, 0.3%, and 0.1% for $Au/CeO_2$, $Pd/CeO_2$, $Pt/CeO_2$, $Rh/CeO_2$, and $Ru/CeO_2$, respectively. Despite using the same initial amount of each metal during synthesis, a variation in metal loading on $CeO_2$ was observed. These differences may arise from variations in metal-support interactions and the intrinsic properties of each metal, such as their charges and interactions in solution, which influence the extent of metal incorporation onto the support surface.

The specific surface areas of pure $CeO_2$ and $M/CeO_2$ catalysts ranged from 77.4 to 122.6 $m^2 \cdot g^{-1}$. Pure $CeO_2$ exhibited a specific surface area of 85.9 $m^2 \cdot g^{-1}$. Following metal incorporation, significant variations in surface area were observed. $Rh/CeO_2$ showed the lowest surface area at 77.4 $m^2 \cdot g^{-1}$, likely due to pore blockage, whereas $Pt/CeO_2$ exhibited the highest surface area at 122.6 $m^2 \cdot g^{-1}$. The observed variability in specific surface area among the $M/CeO_2$ catalysts can be attributed to multiple factors, including metal-support interactions and structural modifications of the $CeO_2$ support induced by metal deposition. For $Rh/CeO_2$, the decrease in specific surface area (77 $m^2.g^{-1}$ versus 85 $m^2.g^{-1}$ for pure $CeO_2$) can be explained by strong metal-support interactions, where Rh nanoparticles are well-dispersed and anchored to $CeO_2$ lattice oxygen, forming small, stable clusters as observed in TEM images. This is further supported by $H_2$-TPR, which shows the lowest reduction temperature for $Rh/CeO_2$, and by CO-TPD, where desorption occurs at lower temperatures (shoulder peak at 250–300 °C), confirming strong Rh-$CeO_2$ interaction. In contrast, $Au/CeO_2$ and $Pd/CeO_2$ exhibit the same specific surface area values (81 $m^2.g^{-1}$), slightly lower than pure $CeO_2$. This can be attributed to partial pore blocking by larger metal nanoparticles (5.9 nm for Au, 4.6 nm for Pd), combined with Au weaker metal-support interactions. $Pt/CeO_2$ and $Ru/CeO_2$ show higher specific surface area (122 and 95 $m^2.g^{-1}$, respectively), due to their ability to stabilize $CeO_2$ oxygen vacancies and enhance surface oxygen mobility, preventing support sintering. This is corroborated by significant changes in their $H_2$-TPR profiles compared to pure $CeO_2$.

The metallic surface area and metal dispersion, measured by CO chemisorption, revealed that the specific metal surface area decreased in the order: $Au/CeO_2 \sim Ru/CeO_2 > Pd/CeO_2 > Pt/CeO_2 \sim Rh/CeO_2$. In contrast, metal dispersion decreased in the order: $Rh/CeO_2 > Au/CeO_2 > Pt/CeO_2 > Ru/CeO_2 > Pd/CeO_2$.[35–39] Catalyst reducibility, as measured by $H_2$-TPR, increased in the following order: $CeO_2 < Au/CeO_2 < Rh/CeO_2 < Pt/CeO_2 < Pd/CeO_2 < Ru/CeO_2$.

Interesting insights were obtained from hydrogen temperature-programmed reduction ($H_2$-TPR) and CO temperature-programmed desorption (CO-TPD) studies, as shown in Figures 5 and 6, respectively. The reducibility of the $CeO_2$ support is a critical parameter for catalytic applications. Noble metals are known to strongly interact with metal oxides, modifying their redox properties and significantly influencing catalytic activity. Previous studies showed that $CeO_2$ exhibits two or three peaks associated with the reduction of surface and bulk oxides. The first peak, observed at temperatures below 500 °C, corresponds to the reduction of surface oxides and active oxygen species. The second peak, typically appearing between 500 °C and 650 °C, is attributed to the reduction of non-stoichiometric composition of $Ce_yO_{2-x}$. The third peak, occurring at temperatures above 800 °C, is linked to the bulk reduction of $CeO_2$ to $Ce_2O_3$.[40–42]

Figure 5A shows that The $CeO_2$ support exhibits three distinct reduction peaks in $H_2$-TPR profiles at 194 °C, 612 °C, and 890 °C. The low-intensity peak at 194 °C corresponds to the

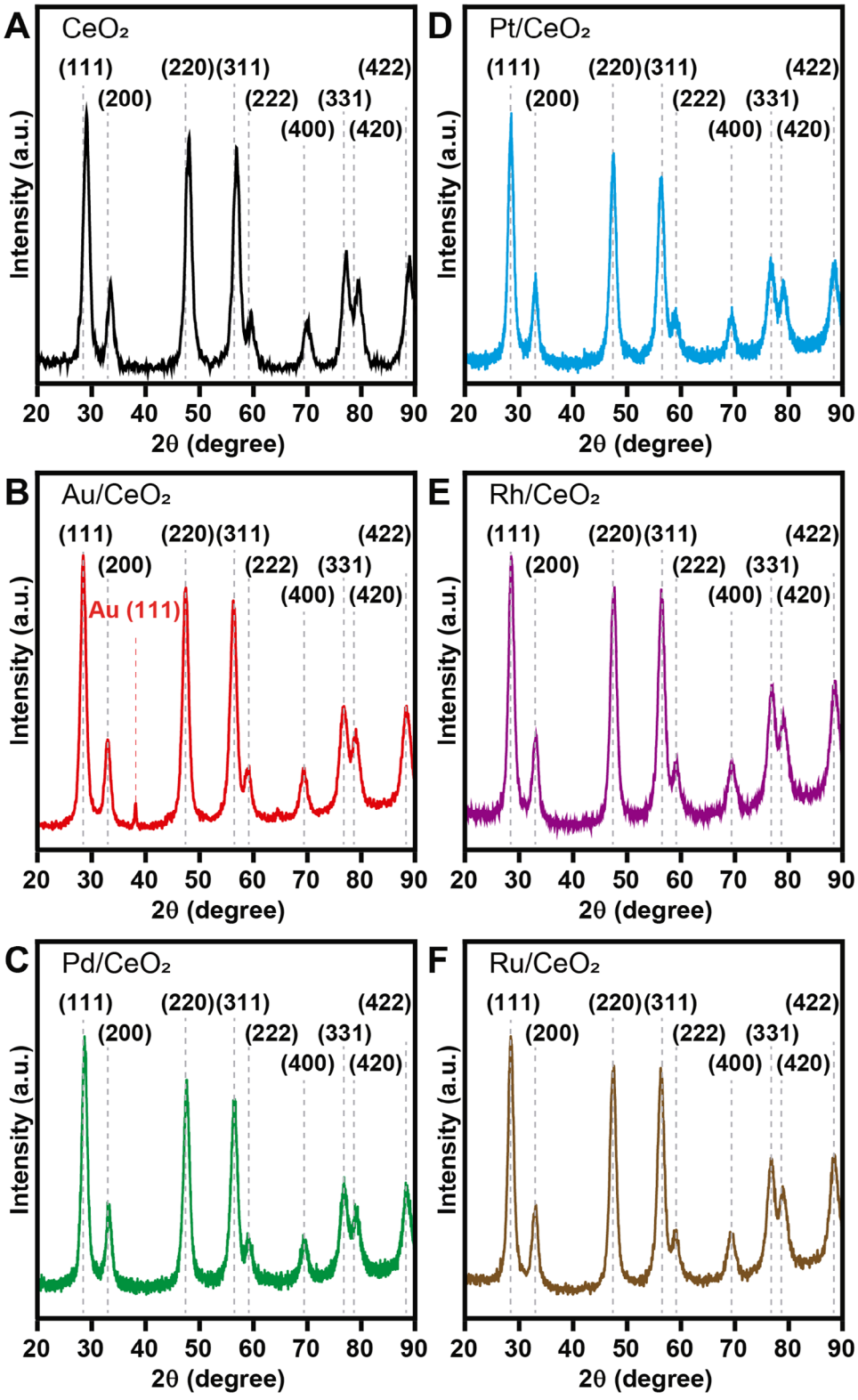


**Figure 4.** (A) XRD diffraction of $CeO_2$, (B) $Au/CeO_2$, (C) $Pd/CeO_2$, (D) $Pt/CeO_2$, (E) $Rh/CeO_2$, and (F) $Ru/CeO_2$ catalysts.

reduction of weakly bound surface oxygen species, indicating a relatively low concentration of oxygen vacancies in the pristine $CeO_2$ support.[43,44] Quantitative analysis of $H_2$ consumption, summarized in Table 1, reveals significant changes in reducibility after metal deposition, as clearly shown in Figure 5B–F.

For the low-temperature region (<500 °C), all metal-loaded catalysts display one or two reduction events associated with surface modifications of $CeO_2$. These events reflect enhanced oxygen mobility and generation of active oxygen species at the metal-support interface.[45–47] Notably, catalysts showing lower

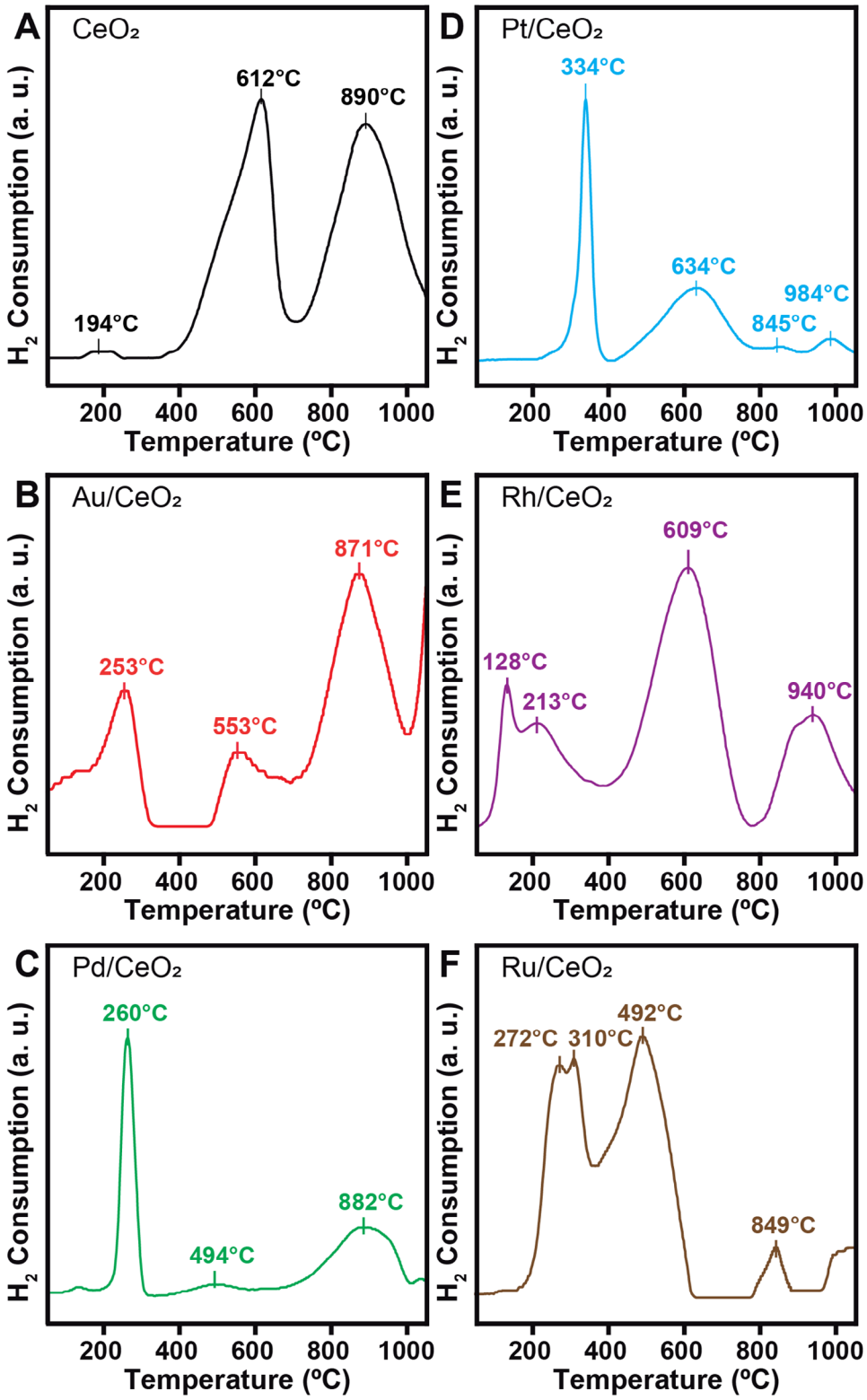


**Figure 5.** (A) $H_2$-TPR profiles of $CeO_2$, (B) $Au/CeO_2$, (C) $Pd/CeO_2$, (D) $Pt/CeO_2$, (E) $Rh/CeO_2$, and (F) $Ru/CeO_2$ catalysts.

peak intensities and higher reduction temperatures in this region typically exhibit weaker metal-support interactions, suggesting limited electronic coupling between the metal nanoparticles and the $CeO_2$ surface.[48–50]

The intermediate (500–650 °C) and high-temperature (>650 °C) reduction regions provide critical insights into the redox properties and electron transfer processes.[48,50] An intense second peak signifies strong metal-support interaction, character-

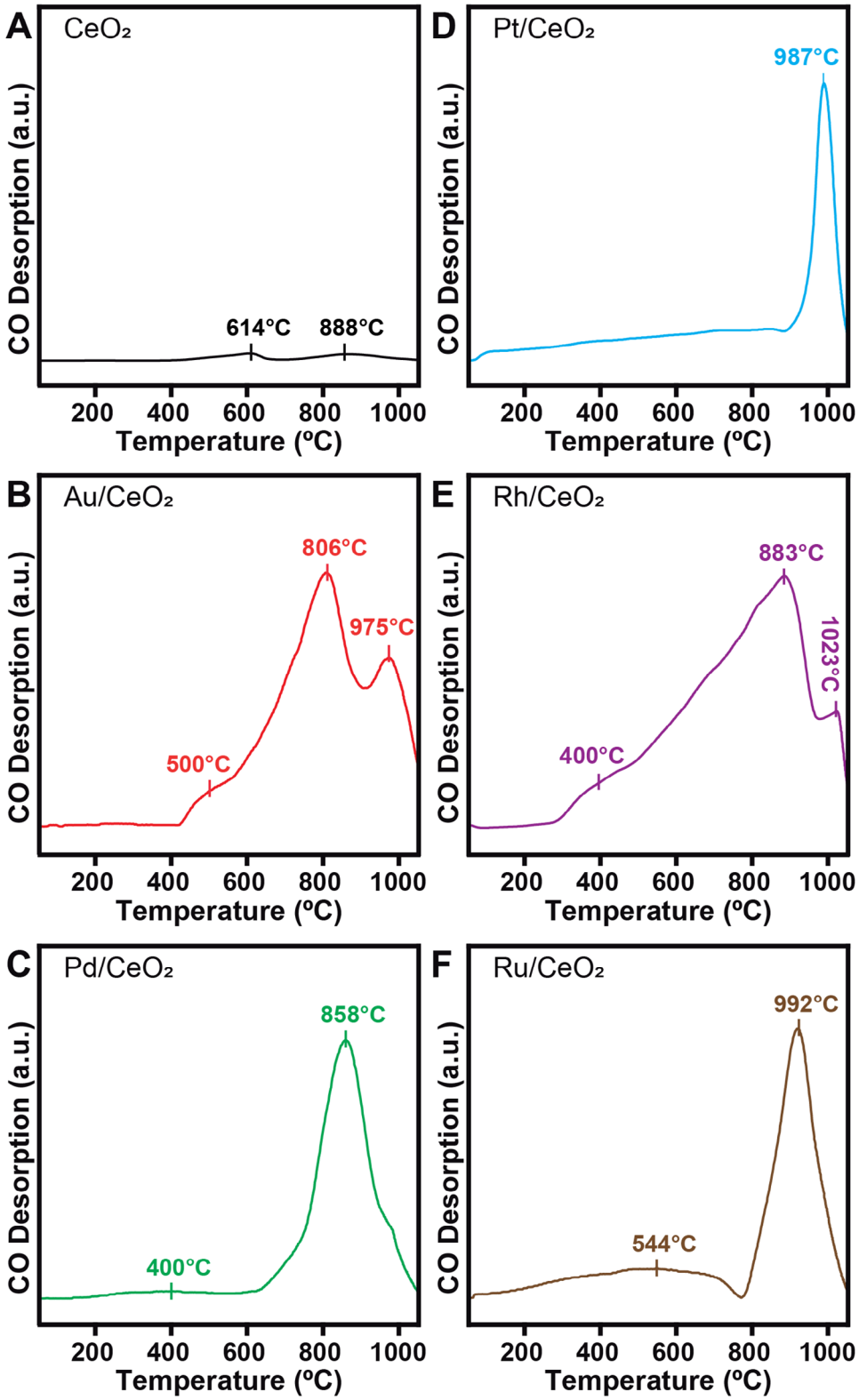


**Figure 6.** (A) CO-TPD profiles of $CeO_2$, (B) $Au/CeO_2$, (C) $Pd/CeO_2$, (D) $Pt/CeO_2$, (E) $Rh/CeO_2$, and (F) $Ru/CeO_2$ catalysts.

ized by metal-induced activation of subsurface oxygen mobility through vacancy creation and stabilization of $Ce^{3+}/Ce^{4+}$ mixed states.[51,52] Conversely, suppression of the third peak indicates very strong metal-support interaction, where electron donation from metal to $CeO_2$ lattice prevents bulk reduction while maintaining optimal oxygen vacancy gradients at the interface.[53–55]

Examining individual systems: $Au/CeO_2$ shows moderate reducibility (19.6%) at 253 °C with weak second and intense

third peaks, consistent with limited metal-support interaction. $Pd/CeO_2$ demonstrates higher low-temperature reducibility (45.1% at 260 °C) but suppressed subsurface reduction, indicating moderate interaction strength. $Pt/CeO_2$ exhibits strong interaction characteristics with surface-dominated reduction (41.3% at 334 °C) and bulk stabilization. $Rh/CeO_2$ stands out with exceptional interfacial properties (33.7% reducibility via dual low-temperature peaks) and balanced surface-bulk redox behavior, confirming very strong metal-support interaction. $Ru/CeO_2$ shows unique behavior with high reducibility (76.5%) but delayed reduction kinetics due to $RuO_x$-$CeO_2$ interface formation, representing a distinct type of strong interaction.

The CO-TPD profiles presented in Figure 6 offer insights into the surface properties of $M/CeO_2$ catalysts, elucidating distinct CO adsorption and desorption behaviors that correlate with metal dispersion characteristics, acid-base properties, and metal-support interaction strength.[56,57] CO adsorption occurs preferentially on three types of sites: metallic centers ($M^0$-CO), Lewis acid sites (including $Ce^{4+}$ and metal cations), and oxygen vacancy defects.[57,58] The $CeO_2$ support itself exhibits two characteristic desorption features at 614 °C and 888 °C, corresponding respectively to CO interactions with surface oxygen vacancies (acting as weak Lewis acid sites) and bulk reduction processes involving the $Ce^{4+}$ to $Ce^{3+}$ transition.[56,59]

The $Au/CeO_2$ reveals three distinct desorption features that provide insight into the surface properties of catalyst. A shoulder at 500 °C corresponds to weak CO adsorption on metallic Au nanoparticles ($Au^0$), demonstrating limited interaction between Au and the $CeO_2$ support.[60] The prominent peak at 806 °C indicates CO binding to defective $CeO_2$ sites near Au-$CeO_2$ interfaces, representing Lewis acid-base pair interactions. A medium-intensity peak at 975 °C suggests CO interaction with bulk $CeO_2$ reduction processes.[60] These observations collectively indicate that CO adsorption occurs predominantly on support defects rather than Au nanoparticles, reflecting weak metal-support interaction.

The $Pd/CeO_2$ profile shows minimal low-temperature activity and a single dominant peak at 858 °C, characteristic of CO desorption from aggregated Pd particles in bridged or multi-coordinated configurations.[61] This observation suggests poor metal dispersion and limited interfacial sites. In contrast, $Pt/CeO_2$ displays an intense single desorption peak at 987 °C, indicating strong CO binding to Pt sites with significant electron density transfer to the $CeO_2$ support.[62] Although this demonstrates substantial metal-support interaction, it may also result in CO poisoning during catalytic reactions. $Rh/CeO_2$ presents a more complex profile, with broad desorption between 300–883 °C encompassing multiple adsorption environments ($Rh^0$ nanoparticles, $Rh^{3+}$ Lewis acid sites, and Rh-$CeO_2$ interfaces) and a minor high-temperature peak at 1023 °C corresponding to CO interaction with deeply reduced ceria.[63,64]

The $Ru/CeO_2$ system exhibits bimodal desorption behavior, with a broad low-temperature feature (100–544 °C) associated with both $RuO_x$ species and metallic $Ru^0$, and an intense high-temperature peak (992 °C) representing CO bound to bulk-like $Ru^0$ or Ru-$Ce^{3+}$ interfaces.[65] The results demonstrate how metal selection significantly influences the surface chemistry of ceria-supported catalysts. The CO-TPD data reveal three key parameters: metal dispersion quality follows the order Rh > Pt > Ru > Pd > Au; Lewis acidity strength decreases as Ru > Rh > Pd > Au ≈ Pt; and metal-support interaction strength varies as Rh ≈ Pt > Ru > Pd > Au.

Pure $CeO_2$ was tested for comparison, and the results are presented in Figure 7A. In the initial reaction phase, the observed high ethanol conversion (100%) and significant ethene production (40%) demonstrate that dehydration reactions dominate, as described by Equation 10. This behavior occurs because fresh $CeO_2$ contains $Ce^{4+}$ cations (Lewis acid sites) and $O^{2-}$ anions (Lewis base sites).[66–68] Ethanol adsorbs dissociatively on the $CeO_2$ surface through a dehydrogenation process, forming adsorbed ethoxy species ($CH_3CH_2OH \rightarrow CH_3CH_2O^* + H$), which subsequently undergo dehydroxylation to produce ethene ($CH_3CH_2O \rightarrow CH_2CH_{2(g)} + OH^*$).[69–72]

As the reaction progresses, the $CeO_2$ surface undergoes partial reduction ($Ce^{4+} \rightarrow Ce^{3+}$), leading to an increase in oxygen vacancy concentration and enhanced basic site density (strong Lewis basicity).[73,74] This transformation induces carbon deposition, which partially blocks active sites.[75,76] These modifications promote dehydrogenation pathways over dehydration, resulting in a shift in selectivity toward acetaldehyde. The growing number of oxygen vacancies facilitate ethanol dehydrogenation to acetaldehyde (Equation 11), while simultaneously suppressing ethene formation via dehydration.[72,77]

The decline in ethanol conversion correlates directly with the increasing acetaldehyde trend due to three key factors. First, acetaldehyde exhibits greater stability than ethanol on the progressively reduced $CeO_2$ surface, leading to product inhibition.[72,73,77] Second, carbonaceous species accumulate on active sites, particularly those responsible for complete reforming. Third, the reduction of $CeO_2$ diminishes its oxygen exchange capacity, which is essential for cleaving C—C bonds in subsequent acetaldehyde reforming steps.[72–74] This establishes a self-reinforcing cycle in which acetaldehyde production rises while overall conversion declines, as the catalyst surface increasingly favors dehydrogenation over complete reforming.

After the metal incorporation, the $M/CeO_2$ catalysts (Figure 7B–F) showed that the metal promotes different reactions, making them more selective for specific reactions. The ethanol conversion (Figure 8A) followed the order: $Pt/CeO_2 = Rh/CeO_2 = Ru/CeO_2 > Pd/CeO_2 > Au/CeO_2$. The $H_2$ production (Figure 8B) followed the order: $Rh/CeO_2 > Pt/CeO_2 > Ru/CeO_2 >> Pd/CeO_2 > Au/CeO_2$, with average values of 37.8%, 34.6%, 31.2%, 4.8%, and 3.1%, respectively. These results are associated with the metal-support interaction, chemical nature of the metals, and their intrinsic ability to cleavage of C—C and C—H bonds in ethanol.[13,78] The $Pt/CeO_2$ (Figure 7D), $Rh/CeO_2$ (Figure 7E), and $Ru/CeO_2$ (Figure 7F) catalysts demonstrated good ethanol conversions, $H_2$ production, and stability during the reaction. In the presence of these catalysts, $H_2$ and $CO_2$ were produced by ethanol steam reforming (Equation 1). In the case of $Rh/CeO_2$, CO was obtained due to incomplete ethanol steam reforming (Equation 12). For $Pt/CeO_2$ and $Ru/CeO_2$, CO and $CH_4$ were obtained

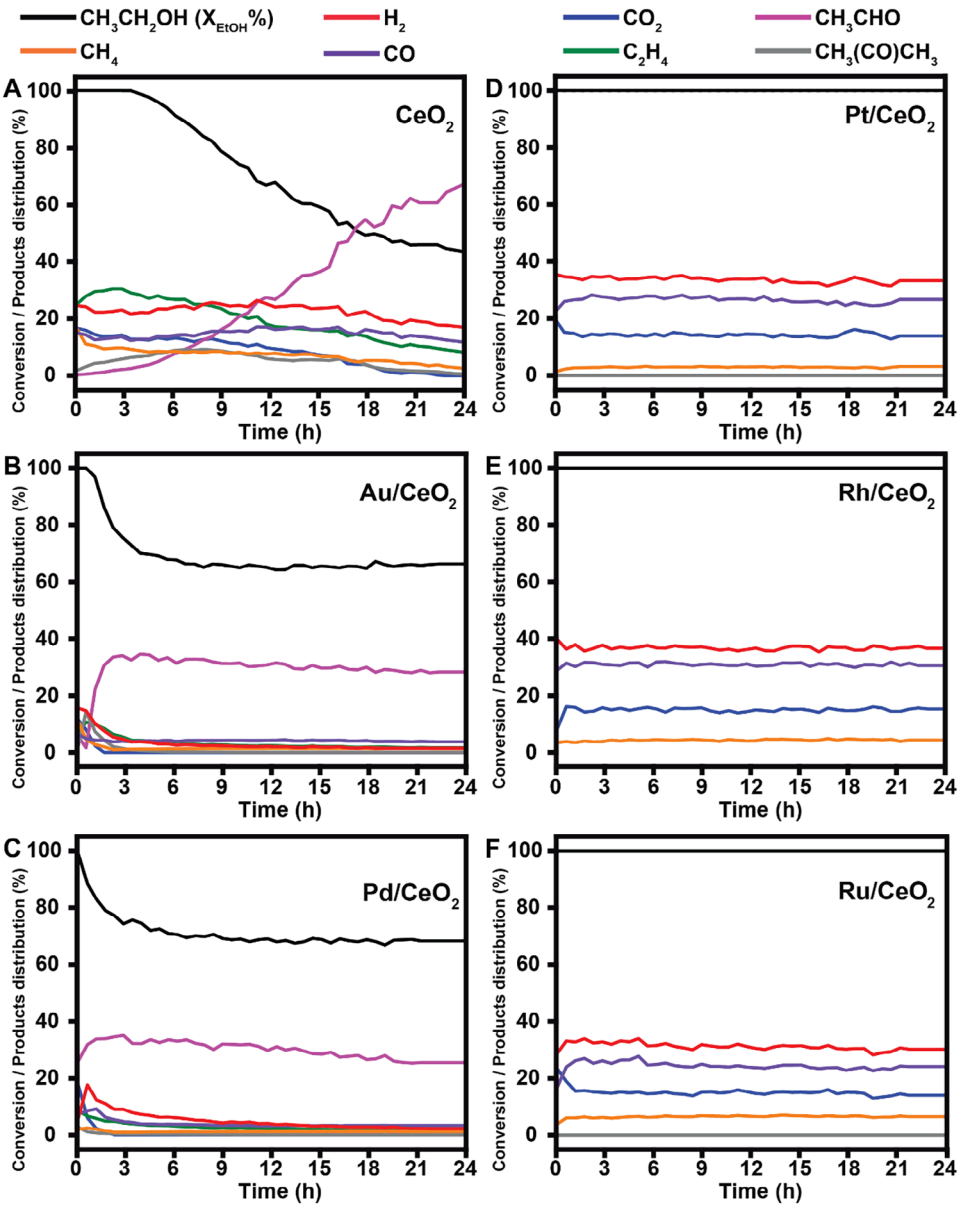


**Figure 7.** Catalytic reaction tests show ethanol conversion, products production, and $H_2$ yield employing pure (A) $CeO_2$, (B) $Au/CeO_2$, (C) $Pd/CeO_2$, (D) $Pt/CeO_2$, (E) $Rh/CeO_2$, and (F) $Ru/CeO_2$ as catalysts.

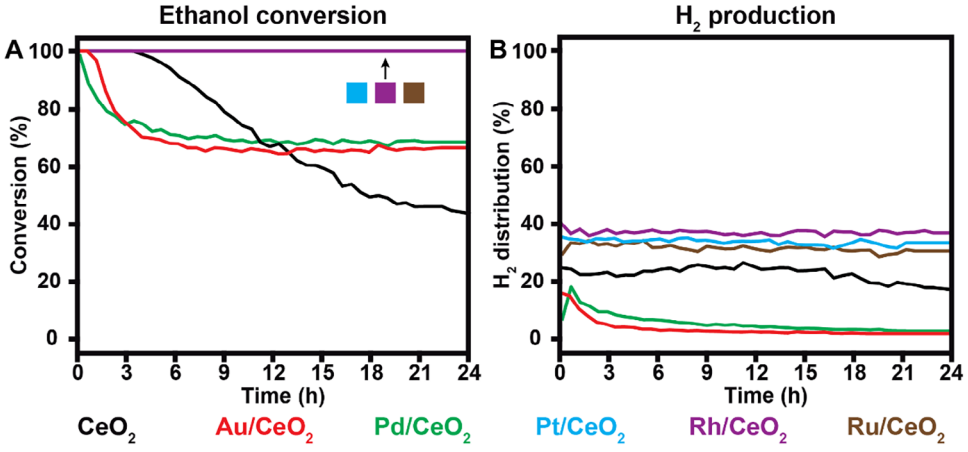


**Figure 8.** (A) Ethanol conversion and (B) $H_2$ production for $CeO_2$ and $M/CeO_2$ catalysts.

from the ethanol decomposition reaction (Equation 13). In contrast, with $Au/CeO_2$ (Figure 7B) and $Pd/CeO_2$ (Figure 7C), the ethanol conversion decreased from the start and stabilized at 65% and 68%, respectively. These metals primarily promoted the dehydrogenation reaction, resulting in a high amount of acetaldehyde produced (Equation 11), with average values of 29.2% for $Au/CeO_2$ and 29.8% for $Pd/CeO_2$. It may be attributed to the strong metal-support interaction and enhanced redox properties as discussed in $H_2$-TPR and CO-TPD to $Pt/CeO_2$, $Rh/CeO_2$, and $Ru/CeO_2$, whereas the low ethanol conversion and low $H_2$ selectivity may $Au/CeO_2$ and $Pd/CeO_2$ depict weak and medium metal-support interaction, respectively.

The influence of metal content is further highlighted by the relationship between metallic surface area, dispersion, and catalytic activity.[79] Metals like Rh, Pt, and Ru, which exhibit higher dispersion on the $CeO_2$ support, created more active sites for ethanol steam reforming. $Rh/CeO_2$ showed exceptional performance, achieving 37.8% hydrogen production and 100% ethanol conversion, due to efficient d-electrons facilitating C—C bond cleavage.[80] In contrast, Pd and Au had lower dispersion and surface activity, resulting in their preferential promotion of dehydrogenation to acetaldehyde rather than the complete reforming of ethanol to hydrogen.[81]

The nature of the metal is another factor that governs the reaction pathways and product selectivity during ethanol steam reforming. Noble metals such as Rh, Pt, and Ru demonstrated superior activity and selectivity due to their intrinsic ability to activate C—C and C—H bonds and their strong interaction with the $CeO_2$ support, enhancing reducibility and oxygen mobility.[70,80] Rh stood out for its ability to cleave C—C bonds efficiently, resulting in 100% ethanol conversion and the highest $H_2$ production. In contrast, Pd and Au, which are more effective at cleavage C—H bonds, showed lower ethanol conversion rates and primarily drove the dehydrogenation reaction, resulting in the formation of acetaldehyde.

Additionally, the reducibility of $M/CeO_2$ catalysts, which is heavily influenced by the metal content to play a significant role in the ethanol steam reforming process. Metals such as Rh, Pt, and Ru enhance the reducibility of $CeO_2$, improving oxygen mobility and facilitating the activation of ethanol molecules. This effect is supported by a downward shift in the $H_2$-TPR reduction peaks and higher hydrogen production observed for these catalysts. On the other hand, the lower reducibility of Au- and Pd-based catalysts led to higher activation barriers for cleavage C—C bonds, favoring partial oxidation and dehydrogenation reactions instead.

The specific surface area of both the support material and the metal is crucial in ethanol steam reforming. BET surface area measurements revealed notable changes after the incorporation of metals. For instance, $Rh/CeO_2$ showed a reduced surface area, likely because of pore blockage. On the other hand, $Pt/CeO_2$ demonstrated the highest surface area, which could improve its catalytic performance by offering more exposed active sites. Similarly, the specific metal surface area, as measured by CO chemisorption, dictates the accessibility of metal nanoparticles for catalytic reactions. Catalysts with higher specific metal surface areas, such as $Rh/CeO_2$, exhibited enhanced catalytic activity, as the higher surface area facilitates ethanol adsorption and the subsequent cleavage of C—C and C—H bonds.

$$C_2H_5OH \rightarrow C_2H_4 + H_2O \quad (10)$$

$$C_2H_5OH \rightarrow C_2H_4O + H_2 \quad (11)$$

$$C_2H_5OH + H_2O \rightarrow 2CO + 4H_2 \quad (12)$$

$$C_2H_5OH \rightarrow CH_4 + CO + H_2 \quad (13)$$

The best results were achieved with $Rh/CeO_2$, which exhibited 37.8% of $H_2$ and 100% ethanol conversion. This is due to the well-established efficiency of Rh for C—C bond dissociation, facilitated by the d-electrons of Rh that activate the C—H $sp^3$ bonds.[13,78,82,83] Following $Rh/CeO_2$, $Pt/CeO_2$ showed the second-best results, with nearly 34.6% of $H_2$ and 100% ethanol conversion. In contrast, a high production of CO and some $CH_4$ were observed due to the ethanol decomposition reaction. This can be attributed to intrinsic barriers in the transfer of the molecular ligand ($CH_3$—) and the cleavage of the C—C bond.[15,78,83] $Ru/CeO_2$ also showed high $H_2$ production, with 31.2% of $H_2$ and 100% ethanol conversion. The high amounts of CO and some $CH_4$ formed can be attributed to the ability of Ru to cleave both the C—C and O—H bonds.[83–85] $Pd/CeO_2$ and $Au/CeO_2$ were the catalysts with the lowest $H_2$ production and ethanol conversion, which can be attributed to the tendency of Pd and Au to form oxidation compounds that facilitate acetaldehyde formation and C—H bond cleavage.[78,81,83,86] It is notable that $Rh/CeO_2$, $Pt/CeO_2$, and $Ru/CeO_2$ are more favorable for promoting reactions that cleave the C—C bond to form $C_1$ compounds. In contrast, $Pd/CeO_2$ and $Au/CeO_2$ favor cleavage of the C—H bond to form $C_2$ compounds, such as acetaldehyde.[84]

After the catalytic reaction, we focused on characterizing the spent catalysts using XRD and TGA, as shown in Figure 9 and Figure 10, respectively. The XRD analysis demonstrates that the $CeO_2$ peaks remain unchanged after the catalytic experiments. The $M/CeO_2$ catalysts show diffraction peaks associated with SiC, which was used as a diluent in catalytic experiments. TGA analysis was employed to investigate the formation of solid carbon compounds, which could form in the presence of metal catalysts supported onto $CeO_2$. Additionally, some reactions may lead to the formation of solid carbon compounds, such as the polymerization of ethene (Equation 14), acetaldehyde (Equation 15), methane decomposition (Equation 16), and the Boudouard reaction (Equation 17). Regarding the catalysts, acetaldehyde formation may result from the decomposition of acetaldehyde (Equation 18), followed by the reactions mentioned above.[6,8–10]

$$C_2H_{4(g)} \rightarrow C_{(s)} \quad (14)$$

$$C_2H_4O_{(g)} \rightarrow C_{(s)} \quad (15)$$

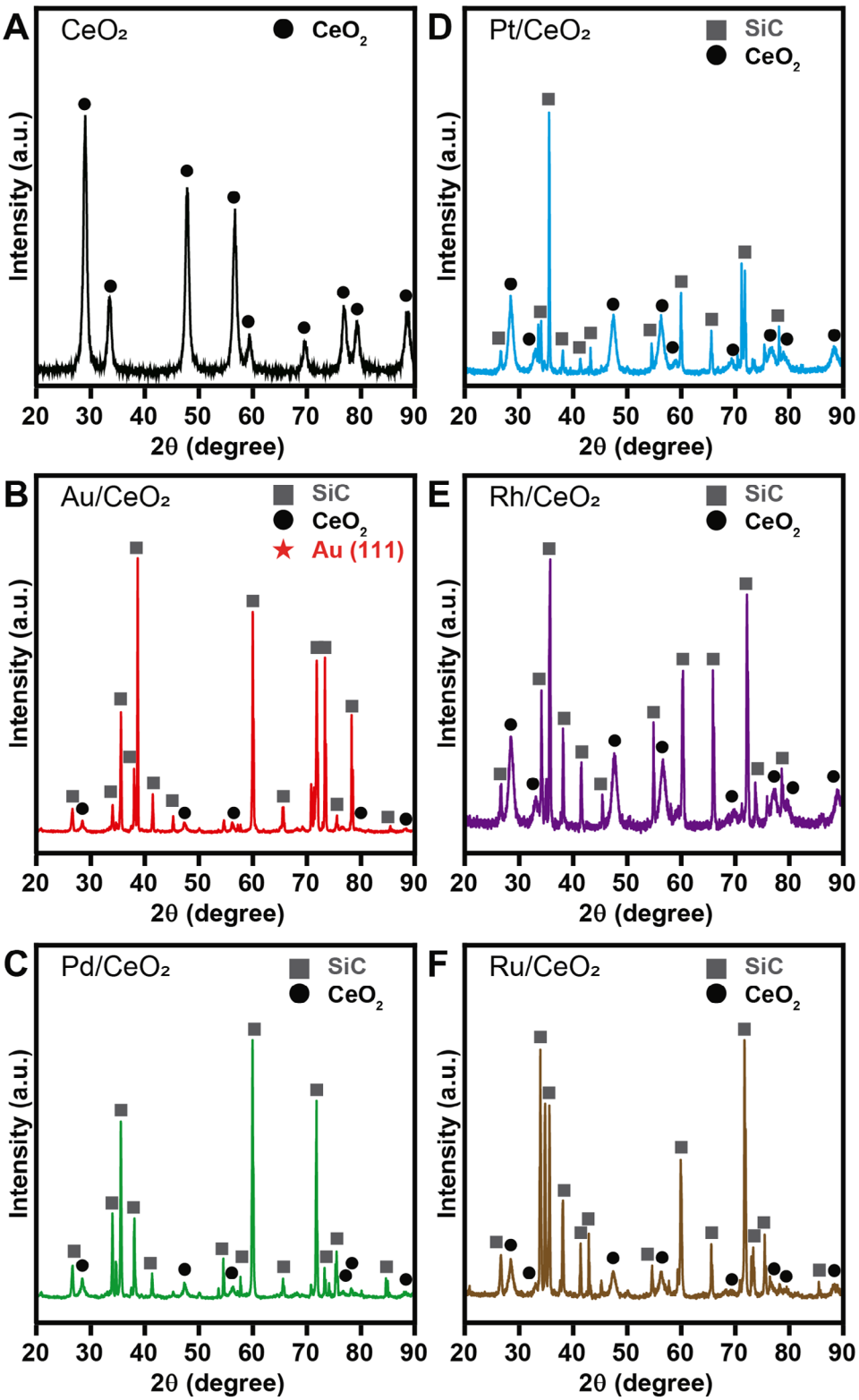


**Figure 9.** XRD spectra of (A) $CeO_2$, (B) $Au/CeO_2$, (C) $Pd/CeO_2$, (D) $Pt/CeO_2$, (E) $Rh/CeO_2$, and (F) $Ru/CeO_2$ catalysts after the ethanol steam reforming experiments.

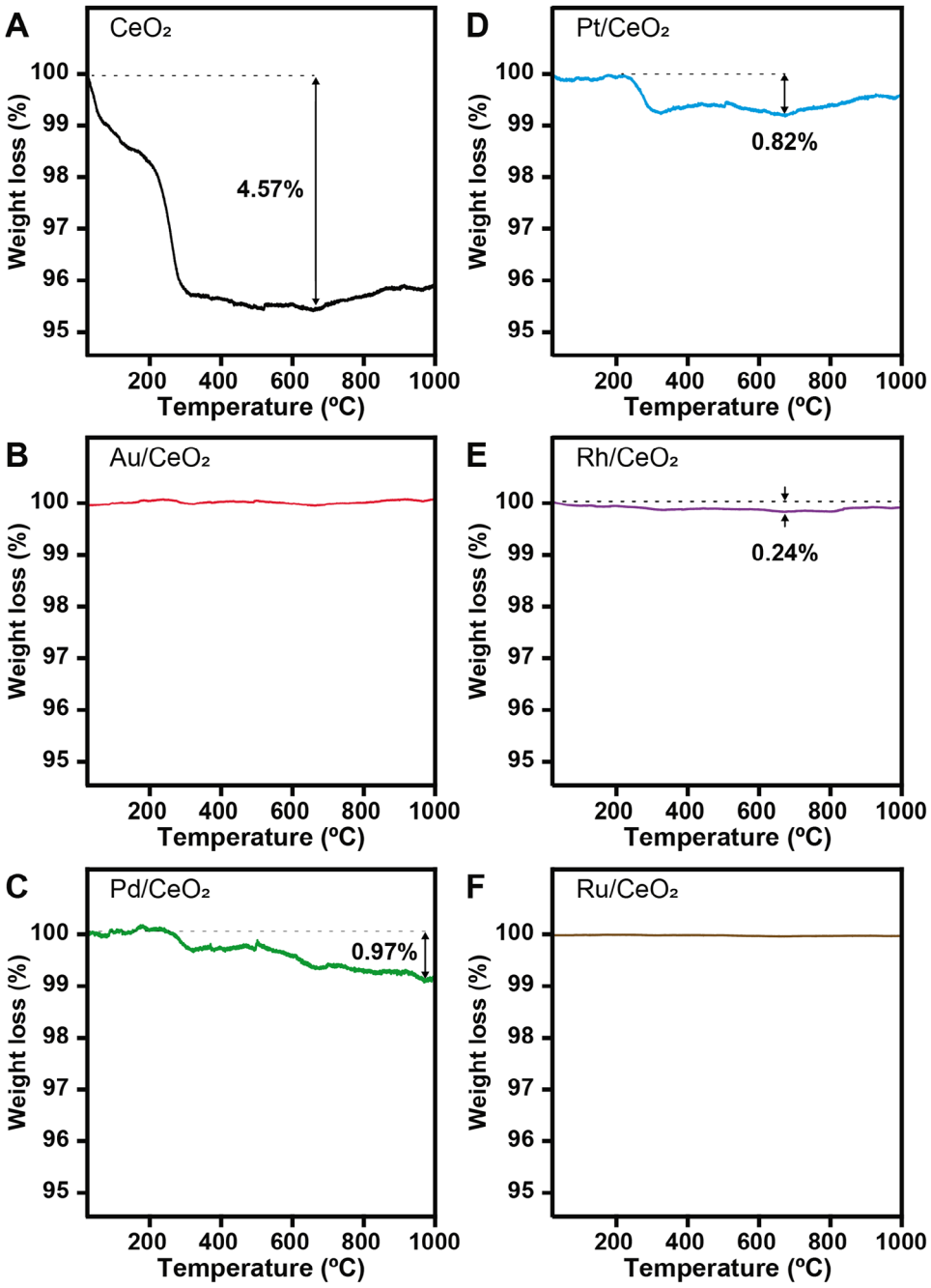


**Figure 10.** TGA profile of (A) $CeO_2$, (B) $Au/CeO_2$, (C) $Pd/CeO_2$, (D) $Pt/CeO_2$, (E) $Rh/CeO_2$, and (F) $Ru/CeO_2$ catalysts after the ethanol steam reforming experiments.

$$CH_{4(g)} \rightarrow 2H_{2(g)} + C_{(s)} \quad (16)$$

$$2\,CO \rightarrow CO_2 + C \quad (17)$$

$$C_2H_4O_{(g)} \rightarrow CH_{4(g)} + CO_{(g)} \quad (18)$$

In the TGA analysis, pure $CeO_2$ (Figure 10) showed a total weight loss of 4.6%, which can be attributed to the decomposition of methane during the first 6 h of reaction, followed by ethene polymerization. After this period, weight loss can be linked to acetaldehyde polymerization, which corresponds to the observed decrease in ethanol conversion after 6 h. The $M/CeO_2$ catalysts exhibited good resistance to carbon compound formation, showing less than 1% weight loss in the TGA analysis. Both $Au/CeO_2$ and $Ru/CeO_2$ showed no significant weight loss, indicating minimal carbon deposition on their surfaces. $Pd/CeO_2$ exhibited a weight loss of 0.97%, which may be attributed to decreased acetaldehyde production, possibly due to acetaldehyde polymerization or the low amounts of $CH_4$ and CO produced, which could result from acetaldehyde decomposition. $Pt/CeO_2$ showed a weight loss of 0.82%,

which can be explained by the high CO production resulting from ethanol decomposition and the low $CH_4$ formation. The modest weight loss is likely due to the decomposition of $CH_4$, which accounts for the higher $H_2$ production compared to $Ru/CeO_2$. $Rh/CeO_2$ exhibited a weight loss of 0.24%, likely due to the Boudouard reaction caused by incomplete steam reforming or the absence of $CH_4$ formation. This absence could result from $CH_4$ decomposition, which in turn enhances $H_2$ production.

To validate the TGA results, carbon balance calculations were performed for all catalysts, yielding average percentages of 80.3% for $CeO_2$, 97.1% for $Au/CeO_2$, 90.2% for $Pd/CeO_2$, 93.2% for $Pt/CeO_2$, 95.6% for $Rh/CeO_2$, and 97.8% for $Ru/CeO_2$. These high carbon recovery percentages (>90% for noble metal catalysts) demonstrate their effectiveness in preventing carbon deposition and minimizing coke accumulation, which is further supported by the minimal weight loss observed in Figure 10.

## 4. Conclusions

The present study describes the synthesis, characterization, and catalytic performance of $CeO_2$-supported $M/CeO_2$ catalysts (M = Au, Pd, Pt, Rh, Ru) for ethanol steam reforming. $CeO_2$ was used as an oxide support with structural stability and catalytic properties for the targeted reaction allowing for the study of the effects of the noble metal. Detailed characterization proved that the deposition of metal nanoparticles was homogeneous, with a minor effect on $CeO_2$ morphology and crystallite size. Reducibility and metal-support interactions showed that the incorporation of noble metals significantly enhances oxygen mobility, decreases the temperature of reduction, and improves catalytic activity. The catalytic tests evidence very distinct $H_2$ production and ethanol conversion depending on the type of noble metal used, with $Rh/CeO_2$ being the most promising catalyst. $Rh/CeO_2$ exhibited the highest hydrogen production (37.8%) and 100% ethanol conversion due to its strong ability in cleaving C—C and C—H bonds. $Pt/CeO_2$ and $Ru/CeO_2$ reached high catalytic efficiency but slightly lower $H_2$ production, along with minor byproducts such as CO and $CH_4$. In contrast, $Pd/CeO_2$, and $Au/CeO_2$ exhibited relatively low ethanol conversion and $H_2$ production, with the primary product being acetaldehyde due to its preferred C—H bond scission in ethanol dehydrogenation. These results again underline the crucial role that the active metal plays in determining catalytic performance: among the tested metals, Rh, Pt, and Ru are ideal candidates for high-performance ethanol steam reforming. The post-reaction characterization showed that negligible carbon deposition occurred on the catalyst surfaces, whereas $Rh/CeO_2$ presented the least weight loss during TGA analyses, indicative of outstanding resistance against carbon formation. The results are aligned with the catalytic stability observed over extended reaction periods. In summary, the study optimizes metal-support interactions and selecting suitable metals to improve catalytic efficiency and durability. These findings offer insights into the development of new catalysts for sustainable hydrogen production via ethanol steam reforming.

## Author Contributions

**Felipe Anchieta e Silva**: Conceptualization; writing—original draft preparation; review; editing; visualization; and project administration. **Eduardo do Espírito Santo Marques**: Data curation. **Fabio Coral Fonseca**: Validation; visualization; and writing—review. **Aleksander Gurlo**: Validation; visualization; and writing—review. **Thenner Silva Rodrigues**: Conceptualization; validation; formal analysis; supervision; project administration; resources and funding acquisition. All authors have read and agreed to the published version of the manuscript.

## Acknowledgements

This work was supported by a research fellowship from the Alexander von Humboldt Foundation. The authors are grateful to the Fundação de Amparo à Pesquisa do Estado do Rio de Janeiro (FAPERJ), Grant Numbers E-26/201.431/2021 and E-26/211.612/2019; to the Conselho Nacional de Desenvolvimento Científico e Tecnológico—CNPq, Grant Number 317288/2021–0, Sis-$H_2$ 407967/2022–2; and to the Coordenação de Aperfeiçoamento de Pessoal de Nível Superior—Brasil (CAPES)—Finance Code 001, Grant Numbers 88881.800240/2022–01, 88887.645934/2021–00 and 88881.934651/2024–01.

## Conflict of Interests

The authors declare no conflict of interest.

## Data Availability Statement

The data that support the findings of this study are available from the corresponding author upon reasonable request.

**Keywords:** Catalytic activity and stability · Cerium oxide support · Ethanol steam reforming · Hydrogen production · Noble metal catalysts

[1] A. Basile, F. Gallucci, A. Iulianelli, S. Tosti, *Fuel Cells* **2008**, *8*, 62–68.
[2] C. Acar, I. Dincer, *J. Clean Prod.* **2019**, *218*, 835–849.
[3] H. F. Abbas, W. M. A. Wan Daud, *Int. J. Hydrogen Energy* **2010**, *35*, 1160–1190.
[4] J. Goldemberg, *Science* **2007**, *315*, 808–810.
[5] J. O. Abe, A. P. I. Popoola, E. Ajenifuja, O. M. Popoola, *Int. J. Hydrogen Energy* **2019**, *44*, 15072–15086.
[6] V. Klouz, V. Fierro, P. Denton, H. Katz, J. P. Lisse, S. Bouvot-Mauduit, C. Mirodatos, *J. Power Sources* **2002**, *105*, 26–34.
[7] M. C. Steil, S. D. Nobrega, S. Georges, P. Gelin, S. Uhlenbruck, F. C. Fonseca *Appl. Energy* **2017**, *199*, 180–186.
[8] L. V. Mattos, G. Jacobs, B. H. Davis, F. B. Noronha, *Chem. Rev.* **2012**, *112*, 4094–4123.
[9] J. L. Contreras, J. Salmones; J. A. Colín-Luna, L. Nuño, B. Quintana, I. Córdova, B. Zeifert, C. Tapia, G. A. Fuentes, *Int. J. Hydrogen Energy* **2014**, *39*, 18835–18853.
[10] M. Ni, D. Y. C. Leung, M. K. H. Leung, *Int. J. Hydrogen Energy* **2007**, *32*, 3238–3247.
[11] Y. C. Sharma, A. Kumar, R. Prasad, S. N. Upadhyay, *Renewable Sustain. Energy Rev.* **2017**, *74*, 89–103.

[12] T. S. Rodrigues, A. B. L. De Moura, F. A. e. Silva, E. G. Candido, A. G. M. Da Silva, D. C. De Oliveira, J. Quiroz, P. H. C. Camargo, V. S. Bergamaschi, J. C. Ferreira, M. Linardi, F. C. Fonseca, *Fuel* **2019**, *237*, 1244–1253.
[13] P. D. Vaidya, A. E. Rodrigues, *Chem. Eng. J.* **2006**, *117*, 39–49.
[14] H. SONG, U. OZKAN, *J. Catal.* **2009**, *261*, 66–74.
[15] A. Ciftci, D. A. J. M. Ligthart, P. Pastorino, E. J. M. Hensen, *Appl. Catal. B* **2013**, *130–131*, 325–335.
[16] F. Wang, L. Zhang, J. Zhu, B. Han, L. Zhao, H. Yu, Z. Deng, W. Shi, *Appl. Catal. A Gen.* **2018**, *564*, 226–233.
[17] L. Soler, A. Casanovas, J. Ryan, I. Angurell, C. Escudero, V. Pérez-Dieste, J. Llorca, *ACS Catal.* **2019**, *9*, 3641–3647.
[18] M. Martinelli, C. D. Watson, G. Jacobs, *Int. J. Hydrogen Energy* **2019**, *45*, 18490-18501.
[19] V. Palma, F. Castaldo, P. Ciambelli, G. Iaquaniello, *Appl. Catal. B* **2014**, *145*, 73–84.
[20] T. S. Rodrigues, F. A. e Silva, E. G. Candido, A. G. M. Da Silva, R. D. S. Geonmonond, P. H. C. Camargo, M. Linardi, F. C. Fonseca, *J. Mater. Sci.* **2019**, *54*, 11400–11416.
[21] M. L. Bosko, N. Ferreira, A. Catena, M. Sergio Moreno, J. F. Múnera, L. Cornaglia, *Catal. Commun.* **2018**, *114*, 19–23.
[22] A. L. Alberton, M. M. V. M. Souza, M. Schmal, *Catal. Today* **2007**, *123*, 257–264.
[23] F. Soyal-Baltacıoğlu, A. E. Aksoylu, Z. I. Önsan, *Catal. Today* **2008**, *138*, 183–186.
[24] H. Wu, B. Yang, *Appl. Surf. Sci.* **2023**, *614*, 156116.
[25] P. Rosha, F. M. Ali, H. Ibrahim, *Can. J. Chem. Eng.* **2023**, *101*, 5498–5518.
[26] D. Gu, J.-C. C. Tseng, C. Weidenthaler, H.-J. J. Bongard, B. Spliethoff, W. Schmidt, F. Soulimani, B. M. Weckhuysen, F. Schüth, *J. Am. Chem. Soc.* **2016**, *138*, 9572–9580.
[27] R. Zanella, S. Giorgio, C. R. Henry, C. Louis, *J. Phys. Chem. B* **2002**, *106*, 7634–7642.
[28] J. P. CHEN, K. ISA, *J. Mass Spectrom. Soc. Jpn.* **1998**, *46*, 299–303.
[29] P. X. Huang, F. Wu, B. L. Zhu, X. P. Gao, H. Y. Zhu, T. Y. Yan, W. P. Huang, S. H. Wu, D. Y. Song, *J. Phys. Chem. B* **2005**, *109*, 19169–19174.
[30] A. G. M. Da Silva, D. C. Batalha, T. S. Rodrigues, E. G. Candido, S. C. Luz, I. C. De Freitas, F. C. Fonseca, D. C. De Oliveira, J. G. Taylor, S. I. Córdoba De Torresi, P. H. C. Camargo, H. V. Fajardo, *Catal. Sci. Technol.* **2018**, *8*, 1828–1839.
[31] A. G. M. da Silva, C. M. Kisukuri, T. S. Rodrigues, E. G. Candido, I. C. de Freitas, A. H. M. da Silva, J. M. Assaf, D. C. Oliveira, L. H. Andrade, P. H. C. Camargo, *Appl. Catal. B* **2016**, *184*, 35–43.
[32] P. M. Schaber, J. Colson, S. Higgins, D. Thielen, B. Anspach, J. Brauer, *Thermochim. Acta* **2004**, *424*, 131–142.
[33] A. C. Basagiannis, P. Panagiotopoulou, X. E. L. Verykios, *Top. Catal.* **2008**, *51*, 2–12.
[34] D. K. Liguras, D. I. Kondarides, X. E. Verykios, *Appl. Catal. B* **2003**, *43*, 345–354.
[35] S. Zhang, X.-S. Li, B. Zhu, J.-L. Liu, X. Zhu, A.-M. Zhu, B. W.-L. Jang, *Catal. Today* **2015**, *256*, 142–147.
[36] H. Yoshida, Y. Onodera, S. Fujita, H. Kawamori, M. Arai, *Green Chem.* **2015**, *17*, 1877–1883.
[37] E. Gallegos-Suarez, A. Guerrero-Ruiz, I. Rodriguez-Ramos, A. Arcoya, *Chem. Eng. J.* **2015**, *262*, 326–333.
[38] P. Kast, M. Friedrich, D. Teschner, F. Girgsdies, T. Lunkenbein, R. Naumann D'alnoncourt, M. Behrens, R. Schlögl, *Appl. Catal. A Gen.* **2015**, *502*, 8–17.
[39] N. Almana, S. P. Phivilay, P. Laveille, M. N. Hedhili, P. Fornasiero, K. Takanabe, J.-M. Basset, *J. Catal.* **2016**, *340*, 368–375.
[40] H. Ding, J. Yang, S. Ma, N. Yigit, J. Xu, G. Rupprechter, J. Wang, *ChemCatChem* **2018**, *10*, 4100–4108.
[41] K. Cheng, W. Song, Y. Cheng, J. Liu, Z. Zhao, Y. Wei, *Catal. Sci. Technol.* **2016**, *6*, 4478–4490.
[42] M. Yin, W. Qiu, L. Song, H. Zhu, Y. Chen, S. Li, J. Cheng, Y. Sun, G. Bai, G. Zhang, H. He, *ChemistrySelect* **2018**, *3*, 2683–2691.
[43] B. Liu, C. Li, Y. Zhang, Y. Liu, W. Hu, Q. Wang, L. Han, J. Zhang, *Appl. Catal. B* **2012**, *111–112*, 467–475.
[44] X.-S. Huang, H. Sun, L.-C. Wang, Y.-M. Liu, K.-N. Fan, Y. Cao, *Appl. Catal. B* **2009**, *90*, 224–232.
[45] H. Eliasson, Y. Niu, R. E. Palmer, H. Grönbeck, R. Erni, *Nanoscale* **2023**, *15*, 19091–19098.
[46] Y. Yu, W. Xia, A. Yu, D. S. A. Simakov, L. Ricardez-Sandoval, *ChemSusChem* **2025**, *18*, e202400681.
[47] S. Turner, S. Lazar, B. Freitag, R. Egoavil, J. Verbeeck, S. Put, Y. Strauven, G. Van Tendeloo, *Nanoscale* **2011**, *3*, 3385.
[48] C. Wang, M. Najimu, B. Ko, E. Sasmaz, *ChemCatChem* **2025**, *17*, e202401449.
[49] R. Alcala, A. Delariva, E. J. Peterson, A. Benavidez, C. E. Garcia-Vargas, D. Jiang, X. I. Pereira-Hernández, H. H. Brongersma, R. T. Veen, J. Staněk, J. T. Miller, Y. Wang, A. Datye, *Appl. Catal. B* **2021**, *284*, 119722.
[50] T. Montini, M. Melchionna, M. Monai, P. Fornasiero, *Chem. Rev.* **2016**, *116*, 5987–6041.
[51] X. Chen, C. Qu, Y. Xiao, W. Wang, J. Zhang, X. Zheng, Q. Ye, *Catal. Today* **2024**, *434*, 114687.
[52] X. Liu, K. Zhou, L. Wang, B. Wang, Y. Li, *J. Am. Chem. Soc.* **2009**, *131*, 3140–3141.
[53] A. Martıńez-Arias, M. Fernández-Garcıá, O. Gálvez, J. M. Coronado, J. A. Anderson, J. C. Conesa, J. Soria, G. Munuera, *J. Catal.* **2000**, *195*, 207–216.
[54] M. López-Haro, J. M. Cíes, S. Trasobares, J. A. Pérez-Omil, J. J. Delgado, S. Bernal, P. Bayle-Guillemaud, O. Stéphan, K. Yoshida, E. D. Boyes, P. L. Gai, J. J. Calvino, *ACS Nano* **2012**, *6*, 6812–6820.
[55] W. Wang, X. Meng, Q. Wang, X.u Jiang, J. Miao, S. Yao, Z. Wu, J. Li, E. Gao, J. Zhu, M. Yao, Q. Dai, *Appl. Catal. B: Environ. Energy* **2025**, *365*, 124912.
[56] B. Liu, C. Li, G. Zhang, L. Yan, Z. Li, *New J. Chem.* **2017**, *41*, 12231–12240.
[57] C. C. Gaioto, J. C. Pinto, M. Schmal, *ACS Omega* **2024**, *9*, 25715–25729.
[58] H. Du, Z. Shao, *Energy Fuels* **2025**, *39*, 5672–5690.
[59] Z.-K. Han, W. Liu, Y. Gao, *JACS Au* 1549-1569, https://doi.org/10.1021/jacsau.5c00095.
[60] O. Bezkrovnyi, A. Bruix, D. Blaumeiser, L. Piliai, S. Schötz, T. Bauer, I. Khalakhan, T. Skála, P. Matvija, P. Kraszkiewicz, M. Pawlyta, M. Vorokhta, I. Matolínová, J. Libuda, K. M. Neyman, L. Kępiński, *Chem. Mater.* **2022**, *34*, 7916–7936.
[61] S. Xie, W. Tan, Y. Xu, C. Wang, Y. Feng, K. Ye, L.u Ma, S. N. Ehrlich, Y. Li, Y. Zhang, L. Dong, J. Deng, F. Liu, *J. Hazard. Mater.* **2024**, *466*, 133632.
[62] E. Groppo, S. Rojas-Buzo, S. Bordiga, *Chem. Rev.* **2023**, *123*, 12135–12169.
[63] E. A. Fedorova, T. Y. Kardash, L. S. Kibis, O. A. Stonkus, E. M. Slavinskaya, V. A. Svetlichnyi, S. Pollastri, A. I. Boronin, *Phys. Chem. Chem. Phys.* **2023**, *25*, 2862–2874.
[64] C. Force, E. Román, J. M. Guil, J. Sanz, *Langmuir* **2007**, *23*, 4569–4574.
[65] X. Qin, X. Chen, M. Chen, J. Zhang, H. He, C. Zhang, *Catal. Sci. Technol.* **2021**, *11*, 1914–1921.
[66] J. Valecillos, S. Iglesias-Vázquez, L. Landa, A. Remiro, J. Bilbao, A. G. Gayubo, *Energy Fuels* **2021**, *35*, 17197–17211.
[67] R. P. Nippes, P. D. Macruz, A. Domingues Gomes, M. de Souza, B. R. Ferreira, R. C. P. Rizzo-Domingues, L. Pereira Ramos, *Processes* **2024**, *12*, 1331.
[68] M. Arapova, S. Naurzkulova, T. Krieger, V. Rogov, V. Sadykov, *Catalysts* **2022**, *12*, 1151.
[69] A. Beste, S. H. Overbury, *J. Phys. Chem. C* **2015**, *119*, 2447–2455.
[70] K. Mudiyanselage, I. Al-Shankiti, A. Foulis, J. Llorca, H. Idriss, *Appl. Catal. B* **2016**, *197*, 198–205.
[71] Y. Choi, M. Scott, T. Söhnel, H. Idriss, *Phys. Chem. Chem. Phys.* **2014**, *16*, 22588–22599.
[72] H. Meng, Y. Yang, T. Shen, W. Liu, L. Wang, P. Yin, Z. Ren, Y. Niu, B. Zhang, L. Zheng, H. Yan, J. Zhang, F.-S. Xiao, M. Wei, X. Duan, *Nat. Commun.* **2023**, *14*, 3189.
[73] M. Shao, X. Bi, Z. Song, Z. Wang, Q. Yang, C. Huang, X. Wang, *ChemCatChem* **2025**, *17*, e202401866.
[74] M. D. Zhurka, J. A. Anderson, A. J. McCue, A. A. Lemonidou, P. N. Kechagiopoulos, *React Chem. Eng.* **2023**, *8*, 2984–2999.
[75] A. Trovarelli, J. Llorca, *ACS Catal.* **2017**, *7*, 4716–4735.
[76] Z. Wu, A. K. P. Mann, M. Li, S. H. Overbury, *J. Phys. Chem. C* **2015**, *119*, 7340–7350.
[77] X. Feng, Y. Zhao, Y. Zhao, H. Wang, H. Liu, Q. A. M. Zhang, *RSC Adv.* **2023**, *13*, 23991–24002.
[78] A. Yee, S. J. Morrison, H. Idriss, *Catal. Today* **2000**, *63*, 327–335.
[79] M. Konsolakis, Z. Ioakimidis, T. Kraia, G. Marnellos, *Catalysts* **2016**, *6*, 39.
[80] A. M. da Silva, K. R. de Souza, G. Jacobs, U. M. Graham, B. H. Davis, L. V. Mattos, F. B. Noronha, *Appl. Catal. B* **2011**, *102*, 94–109.

[81] P.-Y. Sheng, G. A. Bowmaker, H. Idriss, *Appl. Catal. A Gen.* **2004**, *261*, 171–181.
[82] P.-Y. Sheng, A. Yee, G. A. Bowmaker, H. Idriss, *J. Catal.* **2002**, *208*, 393–403.
[83] M. Mavrikakis, M. A. Barteau, *J. Mol. Catal. A Chem.* **1998**, *131*, 135–147.
[84] C.-C. Hung, S.-L. Chen, Y.-K. Liao, C.-H. Chen, J.-H. Wang, *Int. J. Hydrogen Energy* **2012**, *37*, 4955–4966.
[85] C. Chiu, A. Genest, N. Rösch, *Top. Catal.* **2013**, *56*, 874–884.
[86] S. M. Lang, T. M. Bernhardt, V. Chernyy, J. M. Bakker, R. N. Barnett, U. Landman, *Angew. Chem.* **2017**, *129*, 13591–13595.

Manuscript received: March 31, 2025
Revised manuscript received: April 29, 2025
Accepted manuscript online: May 2, 2025
Version of record online: May 15, 2025